Ozone seasonal evolution and photochemical production regime in polluted troposphere in eastern China derived from high resolution FTS observations

Youwen Sun [1, 2)#], Cheng Liu [2, 3, 1)#*], Mathias Palm [4)], Corinne Vigouroux [5)], Justus Notholt [4)], Qihou Hu [1)], Nicholas Jones [6)], Wei Wang [1)], Wenjing Su [3)] , Wenqiang Zhang [3)], Changong Shan [1)], Yuan Tian [1)], Xingwei, Xu [1)], Martine De Mazière [5)], Minqiang Zhou [5)], and Jianguo Liu [1)]

(1 *Key Laboratory of Environmental Optics and Technology, Anhui Institute of Optics and Fine Mechanics, Chinese Academy of Sciences, Hefei 230031, China*)

(2 *Center for Excellence in Urban Atmospheric Environment, Institute of Urban Environment, Chinese Academy of Sciences, Xiamen 361021, China*)

(3 *University of Science and Technology of China, Hefei, 230026, China*)

(4 *University of Bremen, Institute of Environmental Physics, P. O. Box 330440, 28334 Bremen, Germany*)

(5 *Royal Belgian Institute for Space Aeronomy (BIRA-IASB), Brussels, Belgium*)

(6 *School of Chemistry, University of Wollongong, Northfields Ave, Wollongong, NSW, 2522, Australia*)

# These two authors contributed equally to this work

Abstract:

The seasonal evolution of O_3 and its photochemical production regime in a polluted region of eastern China between 2014 and 2017 has been investigated using observations. We used tropospheric ozone (O_3), carbon monoxide (CO) and formaldehyde (HCHO, a marker of VOCs (volatile organic compounds)) partial columns derived from high resolution Fourier transform spectrometry (FTS), tropospheric nitrogen dioxide (NO_2, a marker of NOx (nitrogen oxides)) partial column deduced from Ozone Monitoring Instrument (OMI), surface meteorological data, and a back trajectory cluster analysis technique. A broad O_3 maximum during both spring and summer (MAM/JJA) is observed; the day-to-day variations in MAM/JJA are generally larger than those in autumn and winter (SON/DJF).

Correspondence to: Cheng Liu (chliu81@ustc.edu.cn) or Youwen Sun (ywsun@aiofm.ac.cn)

Tropospheric O_3 columns in June are 1.55×10^{18} molecules*cm^{-2} (56 DU (Dobson Units)) and in December are 1.05×10^{18} molecules*cm^{-2} (39 DU). Tropospheric O_3 columns in June were ~ 50% higher than those in December. Compared with SON/DJF season, the observed tropospheric O_3 levels in MAM/JJA are more influenced by transport of air masses from densely populated and industrialized areas, and the high O_3 level and variability in MAM/JJA is determined by the photochemical O_3 production. The tropospheric column $HCHO/NO_2$ ratio is used as a proxy to investigate the photochemical O_3 production rate (PO_3). The results show that the PO_3 is mainly nitrogen oxides (NO_x) limited in MAM/JJA, while it is mainly VOC or mix VOC-NO_x limited in SON/DJF. Statistics show that NO_x limited, mix VOC-NO_x limited, and VOC limited PO_3 accounts for 60.1%, 28.7%, and 11% of days, respectively. Considering most of PO_3 are NO_x limited or mix VOC-NO_x limited, reductions in NO_x would reduce O_3 pollution in eastern China.

1 Introduction

Human health, terrestrial ecosystems, and materials degradation are impacted by poor air quality resulting from high photochemical ozone (O_3) levels (Wennberg and Dabdub, 2008; Edwards et al., 2013; Schroeder et al., 2017). In polluted areas, tropospheric O_3 generates from a series of complex reactions in the presence of sunlight involving carbon monoxide (CO), nitrogen oxides ($NO_x \equiv$ NO (nitric oxide) + NO_2 (nitrogen dioxide)), and volatile organic compounds (VOCs) (Oltmans et al., 2006; Schroeder et al., 2017). Briefly, VOCs first react with the hydroxyl radical (OH) to form a peroxy radical ($HO_2 + RO_2$) which increases the rate of catalytic cycling of NO to NO_2. O_3 is then produced by photolysis of NO_2. Subsequent reactions between HO_2 or RO_2 and NO lead to radical propagation (via subsequent reformation of OH). Radical termination proceeds via reaction of OH with NOx to form nitric acid (HNO_3) (reaction (1), referred to as LNOx) or by radical-radical reactions resulting in stable peroxide formation (reactions (2) − (4), referred to as LROx, where $ROx \equiv RO_2 + HO_2$) (Schroeder et al., 2017):

$$OH + NO_2 \rightarrow HNO_3 \tag{1}$$

$$2HO_2 \rightarrow H_2O_2 + O_2 \tag{2}$$

60 $$HO_2 + RO_2 \rightarrow ROOH + O_2 \qquad (3)$$

61 $$2RO_2 \rightarrow ROOR + O_2 \qquad (4)$$
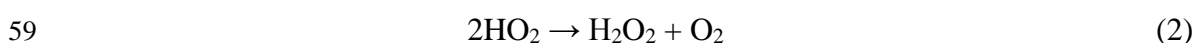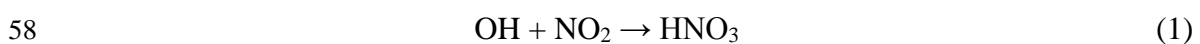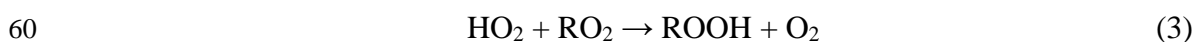
62 Typically, the relationship between these two competing radical termination processes

63 (referred to as the ratio LRO_x/LNO_x) can be used to evaluate the photochemical

64 regime. In high-radical, low-NO_x environments, reactions (2) – (4) remove radicals at

65 a faster rate than reaction (1) (i.e., LROx $\gg$ LNOx), and the photochemical regime is

66 regarded as "NOx limited". In low-radical, high-NOx environments the opposite is

67 true (i.e., LROx $\ll$ LNOx) and the regime is regarded as "VOC limited". When the

68 rates of the two loss processes are comparable (LNOx $\approx$ LROx), the regime is said to

69 be at the photochemical transition/ambiguous point, i.e., mix VOC-NOx limited

70 (Kleinman et al., 2005; Sillman et al., 1995a; Schroeder et al., 2017).

71   Understanding the photochemical regime at local scales is a crucial piece of

72 information for enacting effective policies to mitigate O_3 pollution (Jin et al., 2017;

73 Schroeder et al., 2017). In order to determine the regime, the total reactivity with OH

74 of the myriad of VOCs in the polluted area has to be estimated (Sillman, 1995a; Xing

75 et al., 2017). In the absence of such information, the formaldehyde (HCHO)

76 concentration can be used as a proxy for VOC reactivity because it is a short-lived

77 oxidation product of many VOCs and is positively correlated with peroxy radicals

78 (Schroeder et al., 2017). Sillman (1995a) and Tonnesen and Dennis (2000) found that

79 in situ measurements of the ratio of HCHO (a marker of VOCs) to NO_2 (a marker of

80 NOx) could be used to diagnose local photochemical regimes. Over polluted areas,

81 both HCHO and tropospheric NO_2 have vertical distributions that are heavily

82 weighted toward the lower troposphere, indicating that tropospheric column

83 measurements of these gases are fairly representative of near surface conditions.

84 Many studies have taken advantage of these favorable vertical distributions to

85 investigate surface emissions of NOx and VOCs from space (Boersma et al., 2009;

86 Martin et al., 2004a; Millet et al., 2008; Streets et al., 2013). Martin et al. (2004a) and

87 Duncan et al. (2010) used satellite measurements of column HCHO/NO_2 ratio to

88 explore tropospheric O_3 sensitivities from space and disclosed that this diagnosis of

89 O_3 production rate (PO$_3$) is consistent with previous finding of surface photochemistry.

90   Witte et al. (2011) used the similar technique to estimate changes in PO_3 to the strict

91   emission control measures (ECMs) during Beijing Summer Olympic Games period in

92   2008. Recent papers have applied the findings of Duncan et al. (2010) to observe O_3

93   sensitivity in other parts of the world (Choi et al., 2012; Witte et al., 2011; Jin and

94   Holloway, 2015; Mahajan et al., 2015; Jin et al., 2017).

95   With in situ measurements, Tonnesen and Dennis (2000) observed a

96   radical-limited environment with $HCHO/NO_2$ ratios < 0.8, a NOx-limited

97   environment with $HCHO/NO_2$ ratios >1.8, and a transition environment with

98   $HCHO/NO_2$ ratios between 0.8 and 1.8. With 3-d chemical model simulations,

99   Sillman (1995a) and Martin et al. (2004b) estimated that the transition between the

100 VOC- and NO_x-limited regimes occurs when the $HCHO/NO_2$ ratio is ~ 1.0. With a

101 combination of regional chemical model simulations and the Ozone Monitoring

102 Instrument (OMI) measurements, Duncan et al. (2010) concluded that O_3 production

103 decreases with reductions in VOCs at column $HCHO/NO_2$ ratio < 1.0 and NO_x at

104 column $HCHO/NO_2$ ratio > 2.0; both NO_x and VOCs reductions decrease O_3

105 production when column $HCHO/NO_2$ ratio lies in between 1.0 and 2.0. With a 0-D

106 photochemical box model and airborne measurements, Schroeder et al. (2017)

107 presented a thorough analysis of the utility of column $HCHO/NO_2$ ratios to indicate

108 surface O_3 sensitivity and found that the transition/ambiguous range estimated via

109 column data is much larger than that indicated by in situ data alone. Furthermore,

110 Schroeder et al. (2017) concluded that many additional sources of uncertainty

111 (regional variability, seasonal variability, variable free tropospheric contributions,

112 retrieval uncertainty, air pollution levels and meteorological conditions) may cause

113 transition threshold vary both geographically and temporally, and thus the results from

114 one region are not likely to be applicable globally.

115   With the rapid increase in fossil fuel consumption in China over the past three

116 decades, the emission of chemical precursors of O_3 (NO_x and VOCs) has increased

117 dramatically, surpassing that of North America and Europe and raising concerns about

118 worsening O_3 pollution in China (Tang et al., 2011; Wang et al., 2017; Xing et al.,

119 2017). Tropospheric O_3 was already included in the new air quality standard as a

120   routine monitoring component (http://www.mep.gov.cn, last access on 23 May 2018),

121   where the limit for the maximum daily 8 h average (MDA8) O_3 in urban and

122   industrial areas is $160\mu g/m^3$ (~ 75 ppbv at 273 K, 101.3 kPa). According to air quality

123   data released by the Chinese Ministry of Environmental Protection, tropospheric O_3

124   has replaced PM2.5 as the primary pollutant in many cities during summer

125   (http://www.mep.gov.cn/, last access on 23 May 2018). A precise knowledge of O_3

126   evolution and photochemical production regime in polluted troposphere in China has

127   important policy implications for O_3 pollution controls (Tang et al., 2011; Xing et al.,

128   2017; Wang et al., 2017).

129   In this study, we investigate O_3 seasonal evolution and photochemical production

130   regime in the polluted troposphere in eastern China with tropospheric O_3, CO and

131   HCHO derived from ground-based high resolution Fourier transform spectrometry

132   (FTS) in Hefei, China, tropospheric NO_2 deduced from the OMI satellite

133   (https://aura.gsfc.nasa.gov/ omi.html, last access on 23 May 2018), surface

134   meteorological data, and a back trajectory cluster analysis technique. Considering the

135   fact that most NDACC (Network for Detection of Atmospheric Composition Change)

136   FTS sites are located in Europe and Northern America, whereas the number of sites in

137   Asia, Africa, and South America is very sparse, and there is still no official NDACC

138   FTS station that covers China (http://www.ndacc.org/, last access on 23 May 2018),

139   this study can not only improve our understanding of regional photochemical O_3

140   production regime, but also contributes to the evaluation of O_3 pollution controls.

141   This study concentrates on measurements recorded during midday, when the

142   mixing layer has largely been dissolved. All FTS retrievals are selected within ± 30

143   min of OMI overpass time (13:30 local time (LT)). While the FTS instrument can

144   measure throughout the whole day, if not cloudy, OMI measures only during midday.

145   For Hefei, this coincidence criterion is a balance between the accuracy and the

146   number of data points.

147   **2 Site description and instrumentation**

148   The FTS observation site (117°10′E, 31°54′N, 30 m a.s.l. (above sea level)) is

149   located in the western suburbs of Hefei city (the capital of Anhui Province, 8 million

150   population) in central-eastern China (Figure S1). Detailed description of this site and

151   its typical observation scenario can be found in Tian et al. (2018). Similar to other

152   Chinese megacities, serious air pollution is common in Hefei throughout the whole

153   year (http://mep.gov.cn/, last access on 23 May 2018).

154   Our observation system consists of a high resolution FTS spectrometer

155   (IFS125HR, Bruker GmbH, Germany), a solar tracker (Tracker-A Solar 547, Bruker

156   GmbH, Germany), and a weather station (ZENO-3200, Coastal Environmental

157   Systems, Inc., USA). The near infrared (NIR) and middle infrared (MIR) solar spectra

158   were alternately acquired in routine observations (Wang et al., 2017). The MIR

159   spectra used in this study are recorded over a wide spectral range (about $600 - 4500$

160   cm^{-1}) with a spectral resolution of $0.005 cm^{-1}$. The instrument is equipped with a KBr

161   beam splitter & MCT detector for O_3 measurements and a KBr beam splitter & InSb

162   detector for other gases. The weather station includes sensors for air pressure ($\pm$

163   $0.1 hpa$), air temperature ($\pm 0.3 \,^{\circ}C$), relative humidity ($\pm 3\%$), solar radiation ($\pm 5\%$),

164   wind speed (± 0.2 m/s), wind direction ($\pm 5\,°$), and the presence of rain.

165   ## 3 FTS retrievals of O_3, CO and HCHO

166   ### 3.1 Retrieval strategy

167   The SFIT4 (version 0.9.4.4) algorithm is used in the profile retrieval (Supplement

168   section A; https://www2.acom.ucar.edu/irwg/links, last access on 23 May 2018). The

169   retrieval settings for O_3, CO, and HCHO are listed in Table 1. All spectroscopic line

170   parameters are adopted from HITRAN 2008 (Rothman et al., 2009). A priori profiles

171   of all gases except H_2O are from a dedicated WACCM (Whole Atmosphere

172   Community Climate Model) run. A priori profiles of pressure, temperature and H_2O

173   are interpolated from the National Centers for Environmental Protection and National

174   Center for Atmospheric Research (NCEP/NCAR) reanalysis (Kalnay et al., 1996). For

175   O_3 and CO, we follow the NDACC standard convention with respect to micro

176   windows (MW) selection and the interfering gases consideration (https://www2.acom.

177   ucar.edu/irwg/links, last access on 23 May 2018). HCHO is not yet an official

178   NDACC species but has been retrieved at a few stations with different retrieval

179 settings (Albrecht et al., 2002; Vigouroux et al., 2009; Jones et al., 2009; Viatte et al.,

180 2014; Franco et al., 2015). The four MWs used in the current study are chosen from a

181 harmonization project taking place in view of future satellite validation (Vigouroux et

182 al., 2018). They are centered at around 2770 cm^{-1} and the interfering gases are CH_4,

183 O_3, N_2O, and HDO.

184   We assume measurement noise covariance matrices $\mathbf{S}_\varepsilon$ to be diagonal, and set its

185 diagonal elements to the inverse square of the signal to noise ratio (SNR) of the fitted

186 spectra and its non-diagonal elements to zero. For all gases, the diagonal elements of

187 *a priori* profile covariance matrices $\mathbf{S}_a$ are set to standard deviation of a dedicated

188 WACCM run from 1980 to 2020, and its non-diagonal elements are set to zero.

189   We regularly used a low-pressure HBr cell to monitor the instrument line shape

190 (ILS) of the instrument and included the measured ILS in the retrieval (Hase et al.,

191 2012; Sun et al., 2018).

192 **3.2 Profile information in the FTS retrievals**

193   The sensitive range for CO and HCHO is mainly tropospheric, and for O_3 is both

194 tropospheric and stratospheric (Figure S2). The typical degrees of freedom (DOFS)

195 over the total atmosphere obtained at Hefei for each gas are included in Table 2: they

196 are about 4.8, 3.5, and 1.2 for O_3, CO, and HCHO, respectively. In order to separate

197 independent partial column amounts in the retrieved profiles, we have chosen the

198 altitude limit for each independent layer such that the DOFS in each associated partial

199 column is not less than 1.0. The retrieved profiles of O_3, CO, and HCHO can be

200 divided into four, three, and one independent layers, respectively (Figure S3). The

201 troposphere is well resolved by O_3, CO, and HCHO, where CO exhibits the best

202 vertical resolution with more than two independent layers in the troposphere.

203   In this study, we have chosen the same upper limit (12 km) for the tropospheric

204 columns for all gases (Table 2), which is about 3 km lower than the mean value of the

205 tropopause (~15.1 km). In this way we ensured the accuracies for the tropospheric O_3,

206 CO, and HCHO retrievals, and minimized the influence of transport from stratosphere,

207 i.e., the so called STE process (stratosphere-troposphere exchange).

208 **3.3 Error analysis**

209   The results of the error analysis presented here based on the average of all

210 measurements that fulfill the screening scheme, which is used to minimize the impacts

of significant weather events or instrument problems (Supplement section B). In the troposphere, the dominant systematic error for O_3 and CO is the smoothing error, and for HCHO is the line intensity error (Figure S4). The dominant random error for O_3 and HCHO is the measurement error, and for CO is the zero baseline level error (Figure S5). Taken all error items into account, the summarized errors in O_3, CO, and HCHO for $0-12$ km tropospheric partial column and for the total column are listed in Table 3. The total errors in the tropospheric partial columns for O_3, CO, and HCHO, have been evaluated to be 8.7%, 6.8%, and 10.2%, respectively.

4 Tropospheric O_3 seasonal evolution

4.1 Tropospheric O_3 seasonal variability

Figure 1(a) shows the tropospheric O_3 column time series recorded by the FTS from 2014 to 2017, where we followed Gardiner's method and used a second-order Fourier series plus a linear component to determine the annual variability (Gardiner et al., 2008). The analysis did not indicate a significant secular trend of tropospheric O_3 column probably because the time series is much shorter than those in Gardiner et al. (2008), the observed seasonal cycle of tropospheric O_3 variations is well captured by the bootstrap resampling method (Gardiner et al., 2008). As commonly observed, high levels of tropospheric O_3 occur in spring and summer (hereafter MAM/JJA). Low levels of tropospheric O_3 occur in autumn and winter (hereafter SON/DJF). Day-to-day variations in MAM/JJA are generally larger than those in SON/DJF (Figure 1(b)). At the same time, the tropospheric O_3 column roughly increases over time at the first half of the year and reaches the maximum in June, and then decreases during the second half of the year. Tropospheric O_3 columns in June are 1.55×10^{18} molecules*cm^{-2} (56 DU (Dobson Units)) and in December are 1.05×10^{18} molecules*cm^{-2} (39 DU). Tropospheric O_3 columns in June were ~ 50% higher than those in December.

Vigouroux et al. (2015) studied the O_3 trends and variabilities at eight NDACC FTS stations that have a long-term time series of O_3 measurements, namely, Ny-Ålesund (79 °N), Thule (77 °N), Kiruna (68 °N), Harestua (60 °N), Jungfraujoch (47 °N), Izaña (28 °N), Wollongong (34 °S) and Lauder (45 °S). All these stations

241 were located in non-polluted or relatively clean areas. The tropospheric columns at

242 these stations are of the order of 0.7×10^{18} molecules*cm^{-2} to 1.1×10^{18} molecules*cm^{-2}.

243 The results showed a maximum tropospheric O_3 column in spring at all these stations

244 except at the high altitude stations Jungfraujoch and Izaña where it extended into early

245 summer. This is because the STE process is most effective during late winter and

246 spring (Vigouroux et al. 2015). In contrast, we observed a broader maximum at Hefei

247 which extends over MAM/JJA season, and the values are ~ 35% higher than those

248 studied in Vigouroux et al. (2015). This is because the observed tropospheric O_3 levels

249 in MAM/JJA are more influenced by air masses originated from densely populated

250 and industrialized areas (see section 4.2), and the MAM/JJA meteorological

251 conditions are more favorable to photochemical O_3 production (see section 5.1). The

252 selection of tropospheric limits 3 km below the tropopause minimized but cannot

253 avoid the influence of transport from stratosphere, the STE process may also

254 contribute to high level of tropospheric O_3 column in spring.

4.2 Regional contribution to tropospheric O_3 levels

256 In order to determine where the air masses came from and thus contributed to the

257 observed tropospheric O_3 levels, we have used the HYSPLIT (Hybrid Single-Particle

258 Lagrangian Integrated Trajectory) model to calculate the three-dimensional kinematic

259 back trajectories that coincide with the FTS measurements from 2014 - 2017 (Draxler

260 et al., 2009). In the calculation, the GDAS (University of Alaska Fairbanks GDAS

261 Archive) meteorological fields were used with a spatial resolution of $0.25\degree \times 0.25\degree$, a

262 time resolution of 6 h and 22 vertical levels from the surface to 250 mbar. All daily

263 back trajectories at 12:00 UTC, with a 24 h pathway arriving at Hefei site at 1500 m

264 a.s.l., have been grouped into clusters, and divided into MAM/JJA and SON/DJF

265 seasons (Stunder, 1996). The results showed that air masses in Jiangsu and Anhui

266 Province in eastern China, Hebei and Shandong Province in northern China, Shaanxi,

267 Henan and Shanxi Province in northwestern China, Hunan and Hubei Province in

268 central China contributed to the observed tropospheric O_3 levels.

269 In MAM/JJA season (Figure 2(a)), 28.8% of air masses are east origin and arrived

at Hefei through the southeast of Jiangsu Province and east of Anhui Province; 41.0% are southwest origin and arrived at Hefei through the northeast of Hunan and Hubei Province, and southwest of Anhui Province; 10.1% are northwest origin and arrived at Hefei through the southeast of Shanxi and Henan Province, and northwest of Anhui Province; 10.1% are north origin and arrived at Hefei through the south of Shandong Province and north of Anhui Province; 10.1% are local origin generated in south of Anhui Province. As a result, air pollution from megacities such as Shanghai, Nanjing, Hangzhou and Hefei in eastern China, Changsha and Wuhan in central-southern China, Zhenzhou and Taiyuan in northwest China, and Jinan in north China could contribute to the observed tropospheric O_3 levels.

In SON/DJF season, trajectories are generally longer and originated in the northwest of the MAM/JJA ones (Figure 2(b)). The direction of air masses originating in the eastern sector shifts from the southeast to northeast of Jiangsu Province, and that of local air masses shifts from the south to the northwest of Anhui province. Trajectories of east origin, west origin, and north origin air masses in SON/DJF are 6.5%, 13.1%, and 0.7% less frequent than the MAM/JJA ones, respectively. As a result, the air masses outside Anhui province have 20.2% smaller contribution to the observed tropospheric O_3 levels in SON/DJF than in MAM/JJA. In contrast, trajectories of local origin air masses in SON/DJF are 20.2% more frequent than the MAM/JJA ones, indicating a more significant contribution of air masses inside Anhui province in SON/DJF.

The majority of the Chinese population lives in the eastern part of China, especially in the three most developed regions, the Jing-Jin-Ji (Beijing-Tianjin-Hebei), the Yangtze River Delta (YRD; including Shanghai-Jiangsu-Zhejiang-Anhui), and the Pearl River Delta (PRD; including Guangzhou, Shenzhen, and Hong Kong). These regions consistently have the highest emissions of anthropogenic precursors (Figure S6), which have led to severe region-wide air pollution. Particularly, the Hefei site located in the central-western corner of the YRD, where the population in the southeastern area is typically denser than the northwestern area. Specifically, the southeast of Jiangsu province and the south of Anhui province are two of the most

developed areas in YRD, and human activities therein are very intense. Therefore, when the air masses originated from these two areas, O_3 level is usually very high. Overall, compared with SON/DJF season, the more southeastern air masses transportation in MAM/JJA indicated that the observed tropospheric O_3 levels could be more influenced by the densely populated and industrialized areas, broadly accounting for higher O_3 level and variability in MAM/JJA.

5 Tropospheric O_3 production regime

5.1 Meteorological dependency

Photochemistry in polluted atmospheres, particularly the formation of O_3, depends not only on pollutant emissions, but also on meteorological conditions (Lei et al., 2008; Wang et al., 2016; Coates et al., 2016). In order to investigate meteorological dependency of O_3 production regime in the observed area, we analyzed the correlation of the tropospheric O_3 with the coincident surface meteorological data. Figure 3 shows time series of temperature, pressure, humidity, and solar radiation recorded by the surface weather station. The seasonal dependencies of all these coincident meteorological elements show no clear dependencies except for the temperature and pressure which show clear reverse seasonal cycles. Generally, the temperatures are higher and the pressures are lower in MAM/JJA than those in SON/DJF. The correlation plots between FTS tropospheric O_3 column and each meteorological element are shown in Figure 4. The tropospheric O_3 column shows positive correlations with solar radiation, temperature, and humidity, and negative correlations with pressure.

High temperature and strong sunlight primarily affects O_3 production in Hefei in two ways: speeding up the rates of many chemical reactions and increasing emissions of VOCs from biogenic sources (BVOCs) (Sillman and Samson, 1995b). While emissions of anthropogenic VOCs (AVOCs) are generally not dependent on temperature, evaporative emissions of some AVOCs do increase with temperature (Rubin et al., 2006; Coates et al., 2016). Elevated O_3 concentration generally occurs on days with wet condition and low pressure in Hefei probably because these

329   conditions favor the accumulation of O_3 and its precursors. Overall, MAM/JJA

330   meteorological conditions are more favorable to O_3 production (higher sun intensity,

331   higher temperature, wetter condition, and lower pressure) than SON/DJF, which

332   consolidates the fact that tropospheric O_3 in MAM/JJA are larger than those in

333   SON/DJF.

5.2 PO_3 relative to CO, HCHO, and NO_2 changes

335   In order to determine the relationship between tropospheric O_3 production and its

336   precursors, the chemical sensitivity of PO_3 relative to tropospheric CO, HCHO, and

337   NO_2 changes was investigated. Figure 5 shows time series of tropospheric CO, HCHO,

338   and NO_2 columns that are coincident with O_3 counterparts. The tropospheric NO_2 was

339   deduced from OMI product selected within the $\pm 0.7°$ latitude/longitude rectangular

340   area around Hefei site. The retrieval uncertainty for tropospheric column of is less

341   than 30% (https://disc.gsfc.nasa.gov/datasets/OMNO2_V003/). Tropospheric HCHO

342   and NO_2 show clear reverse seasonal cycles. Generally, tropospheric HCHO are higher

343   and tropospheric NO_2 are lower in MAM/JJA than those in SON/DJF. Pronounced

344   tropospheric CO was observed but the seasonal cycle is not evident probably because

345   CO emission is not constant over season or season dependent.

346   Figure 6 shows the correlation plot between the FTS tropospheric O_3 column and

347   the coincident tropospheric CO, HCHO, and NO_2 columns. The tropospheric O_3

348   column shows positive correlations with tropospheric CO, HCHO, and NO_2 columns.

349   Generally, the higher the tropospheric CO concentration, the higher the tropospheric

350   O_3, and both VOCs and NO_x reductions decrease O_3 production. As an indicator of

351   regional air pollution, the good correlation between O_3 and CO (Figure 6(a)) indicates

352   that the enhancement of tropospheric O_3 is highly associated with the photochemical

353   reactions which occurred in polluted conditions rather than due to the STE process.

354   The relative weaker overall correlations of O_3 with HCHO (Figure 6 (b)) and NO_2

355   (Figure 6 (c)) are partly explained by different lifetimes of these gases, i.e., several

356   hours to 1 day in summer for NO_2 and HCHO, several days to weeks for O_3. So older

357   O_3 enhanced air masses easily loose trace of NO_2 or HCHO. Since the sensitivity of

358   PO$_3$ to VOCs and NO$_x$ is different under different limitation regimes, the relative flat

359   overall slopes indicates that the O$_3$ pollution in Hefei can neither be fully attributed to

360   NO$_x$ pollution nor VOCs pollution.

361   5.3 O$_3$-NOx-VOCs sensitivities

362   5.3.1 Transition/ambiguous range estimation

363   Referring to previous studies, the chemical sensitivity of PO$_3$ in Hefei was

364   investigated using the column HCHO/NO$_2$ ratio (Martin et al., 2004; Duncan et al.,

365   2010; Witte et al., 2011; Choi et al., 2012; Jin and Holloway, 2015; Mahajan et al.,

366   2015; Schroeder et al., 2017; Jin et al., 2017). The methods have been adapted to the

367   particular conditions in Hefei. In particular the findings of Schroeder et.al (2017) have

368   been taken into account.

369   Since the measurement tools for O$_3$ and HCHO, the pollution characteristic and

370   the meteorological condition in this study were not the same as those of previous

371   studies, the transition thresholds estimated in either previous studies were not

372   straightly applied here (Martin et al., 2004a; Duncan et al., 2010; Witte et al., 2011;

373   Choi et al., 2012; Jin and Holloway, 2015; Mahajan et al., 2015; Schroeder et al.,

374   2017; Jin et al., 2017). In order to determine transition thresholds applicable in Hefei,

375   China, we iteratively altered the column HCHO/NO$_2$ ratio threshold and judged

376   whether the sensitivities of tropospheric O$_3$ to HCHO or NO$_2$ changed abruptly. For

377   example, in order to estimate the VOC-limited threshold, we first fitted tropospheric

378   O$_3$ to HCHO that lies within column HCHO/NO$_2$ ratios < 2 (an empirical start point)

379   to obtain the corresponding slope, and then we decreased the threshold by 0.1 (an

380   empirical step size) and repeated the fit, i.e., only fitted the data pairs with column

381   HCHO/NO$_2$ ratios < 1.9. This has been done iteratively. Finally, we sorted out the

382   transition ratio which shows an abrupt change in slope, and regarded this as the

383   VOC-limited threshold. Similarly, the NO$_x$-limited threshold was determined by

384   iteratively increasing the column HCHO/NO$_2$ ratio threshold till the sensitivity of

385   tropospheric O$_3$ to NO$_2$ changed abruptly.

386   The transition threshold estimation with this scheme exploits the fact that O$_3$

387   production is more sensitive to VOCs if it is VOCs-limited and is more sensitive to

388   NO_x if it is NO_x limited, and it exists a transition point near the threshold (Martin et

389   al., 2004). Su et al. (2017) used this scheme to investigate the O_3-NOx-VOCs

390   sensitivities during the 2016 G20 conference in Hangzhou, China, and argued that this

391   diagnosis of PO_3 could reflect the overall O_3 production conditions.

5.3.2 PO_3 limitations in Hefei

393   Through the above empirical iterative calculation, we observed a VOC-limited

394   regime with column $HCHO/NO_2$ ratios < 1.3, a NOx-limited regime with column

395    $HCHO/NO_2$ ratios > 2.8, and a mix VOC-NO_x-limited regime with column

396    $HCHO/NO_2$ ratios between 1.3 and 2.8. Column measurements sample a larger

397   portion of the atmosphere, and thus their spatial coverage are larger than in situ

398   measurements. So the photochemical scene disclosed by column measurement is

399   larger than the in-situ measurement. Specifically, this study reflects the mean

400   photochemical condition of the troposphere.

401   Schroeder et. al. (2017) argued, the column measurements from space have to be

402   used with care because of the high uncertainty and the inhomogeneity of the satellite

403   measurements. This has been mitigated in this study by the following:

404   The FTIR measurements have a much smaller footprint than the satellite

405   measurements. Also we concentrate on measurements recorded during midday, when

406   the mixing layer has largely been dissolved.

407   The measurements are more sensitive to the lower parts of the troposphere, which

408   can be inferred from the normalized AVK's. This reason is simply, that the AVK's

409   show the sensitivity to the column, but the column per altitude decreases with altitude.

410   Figure 7 shows time series of column $HCHO/NO_2$ ratios which varied over a

411   wide range from 1.0 to 9.0. The column $HCHO/NO_2$ ratios in summer are typically

412   larger than those in winter, indicating that the PO_3 is mainly NO_x limited in summer

413   and mainly VOC limited or mix VOC-NO_x limited in winter. Based on the calculated

414   transition criteria, 106 days of observations that have coincident O_3, HCHO, and NO_2

415   counterparts in the reported period are classified, where 57 days (53.8%) are in

MAM/JJA season and 49 days (46.2%) are in SON/DJF season. Table 4 listed the statistics for the 106 days of observations, which shows that NO_x limited, mix VOC-NO_x limited, and VOC limited PO_3 accounts for 60.3% (64 days), 28.3% (30 days), and 11.4% (12 days), respectively. The majority of NO_x limited (70.3%) PO_3 lies in MAM/JJA season, while the majorities of mix VOC-NO_x limited (70%) and VOC limited (75%) PO_3 lie in SON/DJF season. As a result, reductions in NO_x and VOC could be more effective to mitigate O_3 pollution in MAM/JJA and SON/DJF season, respectively. Furthermore, considering most of PO_3 are NO_x limited or mix VOC-NO_x limited, reductions in NO_x would reduce O_3 pollution in eastern China.

6 Conclusion

We investigated the seasonal evolution and photochemical production regime of tropospheric O_3 in eastern China from 2014 – 2017 by using tropospheric O_3, CO and HCHO columns derived from Fourier transform infrared spectrometry (FTS), tropospheric NO_2 column deduced from Ozone Monitoring Instrument (OMI), the surface meteorological data, and a back trajectory cluster analysis technique. A pronounced seasonal cycle for tropospheric O_3 is captured by the FTS, which roughly increases over time at the first half year and reaches the maximum in June, and then it decreases over time at the second half year. Tropospheric O_3 columns in June are 1.55×10^{18} molecules*cm^{-2} (56 DU (Dobson Units)) and in December are 1.05×10^{18} molecules*cm^{-2} (39 DU). Tropospheric O_3 columns in June were ~ 50% higher than those in December. A broad maximum within both spring and summer (MAM/JJA) is observed and the day-to-day variations in MAM/JJA are generally larger than those in autumn and winter (SON/DJF). This differs from tropospheric O_3 measurements in Vigouroux et al. (2015). However, Vigouroux et al. (2015) used measurements at relatively clean sites.

Back trajectories analysis showed that air pollution in Jiangsu and Anhui Province in eastern China, Hebei and Shandong Province in northern China, Shaanxi, Henan and Shanxi Province in northwest China, Hunan and Hubei Province in central China contributed to the observed tropospheric O_3 levels. Compared with SON/DJF

season, the observed tropospheric O_3 levels in MAM/JJA are more influenced by transport of air masses from densely populated and industrialized areas, and the high O_3 level and variability in MAM/JJA is determined by the photochemical O_3 production. The tropospheric column $HCHO/NO_2$ ratio is used as a proxy to investigate the chemical sensitivity of O_3 production rate (PO_3). The results show that the PO_3 is mainly nitrogen oxide (NO_x) limited in MAM/JJA, while it is mainly VOC or mix VOC-NO_x limited in SON/DJF. Reductions in NO_x and VOC could be more effective to mitigate O_3 pollution in MAM/JJA and SON/DJF season, respectively. Considering most of PO_3 are NO_x limited or mix VOC-NO_x limited, reductions in NO_x would reduce O_3 pollution in eastern China.

Acknowledgements

This work is jointly supported by the National High Technology Research and Development Program of China (No. 2016YFC0200800, No. 2017YFC0210002, No. 2016YFC0203302), the National Science Foundation of China (No. 41605018, No.41877309, No. 41405134, No.41775025, No. 41575021, No. 51778596, No. 91544212, No. 41722501, No. 51778596), Anhui Province Natural Science Foundation of China (No. 1608085MD79), Outstanding Youth Science Foundation (No. 41722501) and the German Federal Ministry of Education and Research (BMBF) (Grant No. 01LG1214A). The processing and post processing environment for SFIT4 are provided by National Center for Atmospheric Research (NCAR), Boulder, Colorado, USA. The NDACC networks are acknowledged for supplying the SFIT software and advice. The HCHO micro-windows were obtained at BIRA-IASB during the ESA PRODEX project TROVA (2016-2018) funded by the Belgian Science Policy Office. The LINEFIT code is provided by Frank Hase, Karlsruhe Institute of Technology (KIT), Institute for Meteorology and Climate Research (IMK-ASF), Germany. The authors acknowledge the NOAA Air Resources Laboratory (ARL) for making the HYSPLIT transport and dispersion model available on the Internet. The authors would also like to thank Dr. Jason R. Schroeder and three anonymous referees for useful comments that improved the quality of this paper.

References

Albrecht T., Notholt J., Wolke R., Solberg S., Dye C., Malberg H., Variations of CH_2O and C_2H_2 determined from ground based FTIR measurements and comparison with model results, Adv. Space Res., 29, p. 1713-1718, 2002.

Boersma, K. F., D. J. Jacob, M. Trainic, Y. Rudich, I. DeSmedt, R. Dirksen, and H. J. Eskes (2009), Validation of urban NO_2 concentrations and their diurnal and seasonal variations observed from the SCIAMACHY and OMI sensors using in situ surface measurements in Israeli cities, Atmos. Chem. Phys., 9(12), 3867–3879, doi:10.5194/acp-9-3867-2009.

Choi, Y., H. Kim, D. Tong, and P. Lee (2012), Summertime weekly cycles of observed and modeled NOx and O_3 concentrations as a function of satellite-derived ozone production sensitivity and land use types over the continental United States, Atmos. Chem. Phys., 12(14), 6291–6307, doi:10.5194/acp-12-6291-2012.

Coates J., Mar K. A., Ojha N., Butler T. M.. The influence of temperature on ozone production under varying NOx conditions - a modelling study. Atmospheric Chemistry and Physics. 2016,16(18):11601-15.

Duncan, B.N., et al., 2010. Application of OMI observations to a space-based indicator of NO_x and VOC controls on surface ozone formation. Atmos. Environ. 44, 2213-2223.

Draxler, R. R., Stunder, B., Rolph, G., and Taylor, A.: HYSPLIT_4 User's Guide, via NOAA ARL website. NOAA Air Resources Laboratory, Silver Spring, MD, December 1997, revised January 2009, http://www.arl.noaa.gov/documents/ reports/hysplit_user_guide.pdf (last access: 19 May 2017), 2009.

Edwards, P. M., Young, C. J., Aikin, K., & Degouw, J. A. (2013). Ozone photochemistry in an oil and natural gas extraction region during winter: simulations of a snow-free season in the uintah basin, utah. Atmospheric Chemistry & Physics, 13(17), 8955-8971.

Franco B., Hendrick F., Van Roozendael M., Muller J. F., Stavrakou T., Marais E. A., Retrievals of formaldehyde from ground-based FTIR and MAX-DOAS

503   observations at the Jungfraujoch station and comparisons with GEOS-Chem and

504   IMAGES model simulations. Atmospheric Measurement Techniques. 2015,

505   8(4):1733-56.

506 Gardiner, T., Forbes, A., de Mazière, M., Vigouroux, C., Mahieu, E., Demoulin, P.,

507   Velazco, V., Notholt, J., Blumenstock, T., Hase, F., Kramer, I., Sussmann, R.,

508   Stremme,W., Mellqvist, J., Strandberg, A., Ellingsen, K., and Gauss, M.: Trend

509   analysis of greenhouse gases over Europe measured by a network of ground-based

510   remote FTIR instruments, Atmos. Chem. Phys., 8, 6719–6727, doi:10.5194/

511   acp-8-6719-2008, 2008.

512 Hase, F.: Improved instrumental line shape monitoring for the ground-based,

513   high-resolution FTIR spectrometers of the Network for the Detection of

514   Atmospheric Composition Change, Atmos. Meas. Tech., 5, 603–610,

515   doi:10.5194/amt-5-603-2012,2012.

516 Jin, X., and T. Holloway (2015), Spatial and temporal variability of ozone sensitivity

517   over China observed from the Ozone Monitoring Instrument, J. Geophys. Res.

518   Atmos., 120, 7229–7246, doi:10.1002/2015JD023250.

519 Jin X. M., Fiore A.M., Murray L.T., Valin L.C., Lamsal L.N., Duncan B. Evaluating a

520   Space-Based Indicator of Surface Ozone-NOx-VOC Sensitivity Over Midlatitude

521   Source Regions and Application to Decadal Trends. J Geophys Res-Atmos.

522   2017,122(19):10231-53.

523 Jones N.B., Riedel K., Allan W., Wood S., Palmer P.I., Chance K., et al. Long-term

524   tropospheric formaldehyde concentrations deduced from ground-based fourier

525   transform solar infrared measurements. Atmos Chem Phys. 2009,9(18):7131-42.

526 Kleinman, L., Daum, P., Lee, Y.-N., Nunnermacker, L., Springston, S., Weinstein-

527   Lloyd, J., Rudolph, J., 2005. A comparative study of ozone production in five

528   U.S. metropolitan areas. Journal of Geophysical Research 110, D02301.

529   doi:10.1029/2004JD005096.

530 Kalnay E., Kanamitsu M., Kistler R., et al. (1996) The NCEP/NCAR 40-year

531   reanalysis project. Bulletin of the American Meteorological Society, 77, 437-472.

532 Lei W., Zavala M., de Foy B., Volkamer R., Molina L. T.. Characterizing ozone

533   production and response under different meteorological conditions in Mexico City.

534   Atmospheric Chemistry and Physics. 2008, 8(24):7571-81.

535 Martin, R., Fiore, A., Van Donkelaar, A., 2004a. Space-based diagnosis of surface

536   ozone sensitivity to anthropogenic emissions. Geophysical Research Letters 31,

537   L06120. doi:10.1029/2004GL019416.

538 Martin, R., Parrish, D., Ryerson, T., Nicks, D., Chance, K., Kurosu, T., Jacob, D.,

539   Sturges, E., Fried, A., Wert, B., 2004b. Evaluation of GOME satellite

540   measurements of tropospheric NO_2 and HCHO using regional data from aircraft

541   campaigns in the southeastern United States. Journal of Geophysical Research

542   109, D24307. doi:10.1029/2004JD004869.

543 Millet, D. B., D. J. Jacob, K. F. Boersma, T.-M. Fu, T. P. Kurosu, K. Chance, C. L.

544   Heald, and A. Guenther (2008), Spatial distribution of isoprene emissions from

545   North America derived from formaldehyde column measurements by the OMI

546   satellite sensor, J. Geophys. Res., 113, D02307, doi:10.1029/2007JD008950.

547 Mahajan, A. S., I. De Smedt, M. S. Biswas, S. Ghude, S. Fadnavis, C. Roy, and M.

548   van Roozendael (2015), Inter-annual variations in satellite observations of

549   nitrogen dioxide and formaldehyde over India, Atmos. Environ., 116, 194–201,

550   doi:10.1016/j.atmosenv.2015.06.004.

551 Oltmans S. J., Lefohn A. S., Harris J. M., et al. Long-term changes in tropospheric

552   ozone. Atmospheric Environment, 2006, 40(17):3156-3173.

553 Rothman, L. S., Gordon, I. E., Barbe, A., Benner, D. C., Bernath, P. F., Birk, M.,

554   Boudon, V., Brown, L. R., Campargue, A., Champion, J.-P., Chance, K., Coudert,

555   L. H., Danaj, V., Devi, V. M., Fally, S., Flaud, J.-M., Gamache, R. R., Goldmanm,

556   A., Jacquemart, D., Kleiner, I., Lacome, N., Lafferty, W. J., Mandin, J.-Y., Massie,

557   S. T., Mikhailenko, S. N., Miller, C. E., Moazzen-Ahmadi, N., Naumenko, O. V.,

558   Nikitin, A. V., Orphal, J., Perevalov, V. I., Perrin, A., Predoi-Cross, A., Rinsland, C.

559   P., Rotger, M., Šime. cková, M., Smith, M. A. H., Sung, K., Tashkun, S. A.,

560   Tennyson, J., Toth, R. A., Vandaele, A. C., and Vander Auwera, J.: The Hitran

561   2008 molecular spectroscopic database, J. Quant. Spectrosc. Ra., 110, 533–572,

562   2009.

563   Rubin, J. I., Kean, A. J., Harley, R. A., Millet, D. B., and Goldstein, A. H.:

564   Temperature dependence of volatile organic compound evaporative emissions

565   from motor vehicles, J. Geophys. Res.-Atmos., 111, d03305,

566   doi:10.1029/2005JD006458, 2006.

567   Schroeder, J. R., Crawford, J. H., Fried, A., Walega, J., Weinheimer, A., & Wisthaler,

568   A., et al. (2017). New insights into the column CH_2O/NO_2 ratio as an indicator of

569   near‐surface ozone sensitivity. Journal of Geophysical Research Atmospheres,

570   122(16).

571   Sillman, S., 1995a. The use of NOy, H_2O_2, and HNO_3 as indicators for ozone-NO_x

572   hydrocarbon sensitivity in urban locations. J. Geophys. Res. 100, 14175-14188.

573   Sillman, S. and Samson, P. J.: Impact of temperature on oxidant photochemistry in

574   urban, polluted rural and remote environments, J. Geophys. Res.-Atmos., 100,

575   11497–11508, 1995b.

576   Stunder, B.: An assessment of the Quality of Forecast Trajectories, J. Appl. Meteorol.,

577   35, 1319–1331, 1996.

578   Streets, D. G., et al. (2013), Emissions estimation from satellite retrievals: A review of

579   current capability, Atmos. Environ., 77, 1011–1042,   doi:10.1016/j.atmosenv.

580   2013.05.051.

581   Su W. J., Liu C., Hu Q.H., Fan G.Q., Xie Z.Q., Huang X., Characterization of ozone in

582   the lower troposphere during the 2016 G20 conference in Hangzhou. Sci Rep-Uk.

583   2017,7.

584   Tang, G., Wang, Y., Li, X., Ji, D., & Gao, X. (2011). Spatial-temporal variations of

585   surface ozone and ozone control strategy for northern china. Atmospheric

586   Chemistry & Physics, 11(9), 26057-26109.

587   Tonnesen, G. S., and R. L. Dennis (2000), Analysis of radical propagation efficiency

588   to assess ozone sensitivity to hydrocarbons and NO_2. Long-lived species as

589   indicators of ozone concentration sensitivity, J. Geophys. Res., 105(D7),

590   9227–9241, doi:10.1029/1999JD900372.

591   Tian Y., Sun Y.W., Liu C., Wang W., Shan C. G., Xu X.W., Hu Q.H., Characterisation

592   of methane variability and trends from near-infrared solar spectra over Hefei,

China, Atmospheric Environment, Volume 173, 2018, Pages 198-209, ISSN 1352-2310, https://doi.org/10.1016/j.atmosenv.2017.11.001.

Vigouroux, C., Blumenstock, T., Coffey, M., Errera, Q., Garcá, O., Jones, N. B., Hannigan, J. W., Hase, F., Liley, B., Mahieu, E., Mellqvist, J., Notholt, J., Palm, M., Persson, G., Schneider, M., Servais, C., Smale, D., Thölix, L., and De Mazière, M.: Trends of ozone total columns and vertical distribution from FTIR observations at eight NDACC stations around the globe, Atmos. Chem. Phys., 15, 2915-2933, doi:10.5194/acp-15-2915-2015, 2015.

Vigouroux C., Hendrick F, Stavrakou T, et al. Ground-based FTIR and MAX-DOAS observations of formaldehyde at Réunion Island and comparisons with satellite and model data[J]. Atmospheric Chemistry & Physics, 2009, 9(4):9523-9544.

Vigouroux, C., Bauer Aquino, C. A., Bauwens, M., Becker, C., Blumenstock, T., De Mazière, M., Garcá, O., Grutter, M., Guarin, C., Hannigan, J., Hase, F., Jones, N., Kivi, R., Koshelev, D., Langerock, B., Lutsch, E., Makarova, M., Metzger, J.-M., Müller, J.-F., Notholt, J., Ortega, I., Palm, M., Paton-Walsh, C., Poberovskii, A., Rettinger, M., Robinson, J., Smale, D., Stavrakou, T., Stremme, W., Strong, K., Sussmann, R., Té, Y., and Toon, G.: NDACC harmonized formaldehyde time series from 21 FTIR stations covering a wide range of column abundances, Atmos. Meas. Tech., 11, 5049-5073, https://doi.org/10.5194/amt-11-5049-2018, 2018.

Witte, J.C., Duncan, B.N, Douglass, A.R, Kurosu, T.P, Chance, K et al. "The unique OMI HCHO/NO_2 feature during the 2008 Beijing Olympics: Implications for ozone production sensitivity". Atmospheric Environment. 45.18 2011-06-01. 3103(9).

Viatte C., Strong K., Walker K.A., Drummond J.R. Five years of CO, HCN, C_2H_6, C_2H_2, CH_3OH, HCOOH and H_2CO total columns measured in the Canadian high Arctic. Atmospheric Measurement Techniques. 2014;7(6):1547-70.

Wennberg, P. O., and Dabdub D. Atmospheric chemistry. Rethinking ozone production. Science 319.5870(2008):1624.

Wang T., Xue L. K., Brimblecombe P., Lam Y. F., Li. L., Zhang L. Ozone pollution in

623   China: A review of concentrations, meteorological influences, chemical

624   precursors, and effects. Sci Total Environ. 2017, 575:1582-96.

625 Wang W., Tian Y., Liu C., Sun Y., Liu W., Xie P., et al. Investigating the performance

626   of a greenhouse gas observatory in Hefei, China. Atmos Meas Tech.

627   2017,10(7):2627-43.

628 Xing, C., Liu, C., Wang, S., Chan, K. L., Gao, Y., & Huang, X., et al. (2017).

629   Observations of the vertical distributions of summertime atmospheric pollutants

630   and the corresponding ozone production in shanghai, china. Atmospheric

631   Chemistry & Physics, 17(23), 1-31.

632 **Figs**

633

634 (a)

635
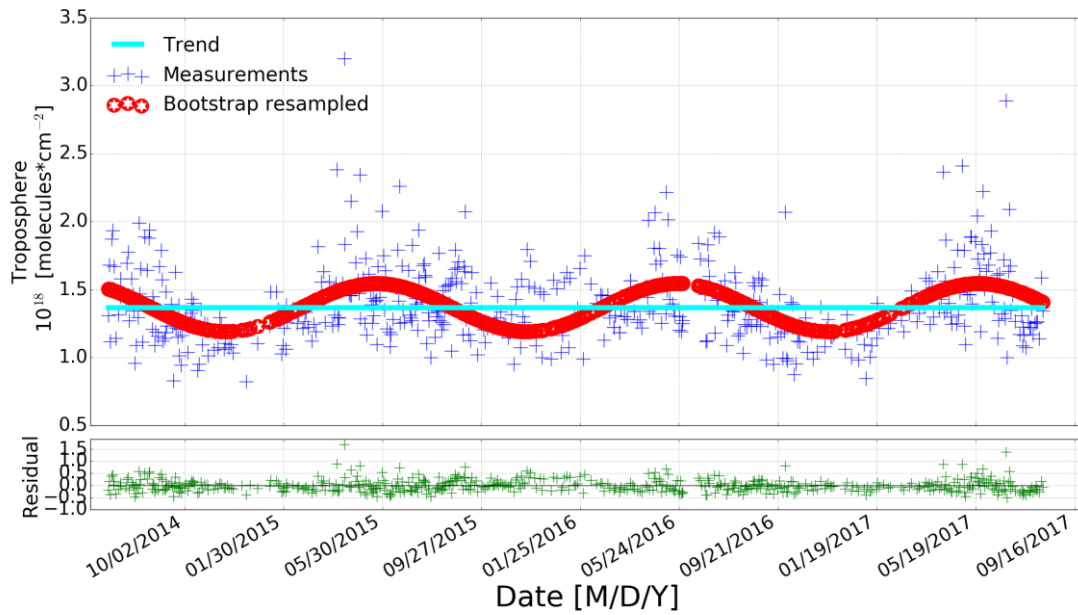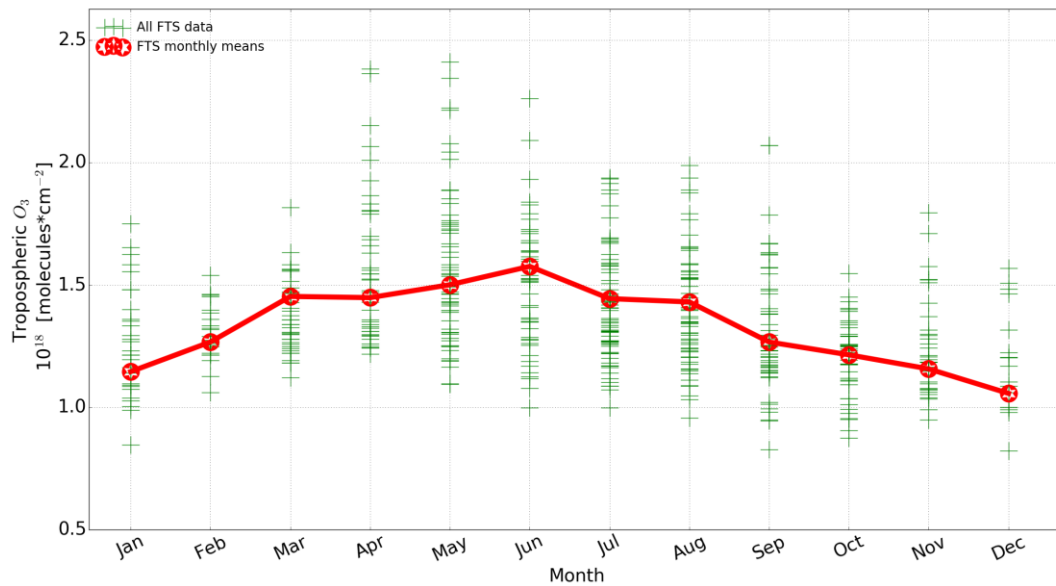
636 (b)

637 Figure 1. (a): FTS measured and bootstrap resampled tropospheric O_3 columns at Hefei site. The
638 linear trend and the residual are also shown. Detailed description of the bootstrap method can be
639 found in Gardiner et al., 2008. (b): Tropospheric O_3 column monthly means derived from (a).

640
641   (a)

642
643   (b)
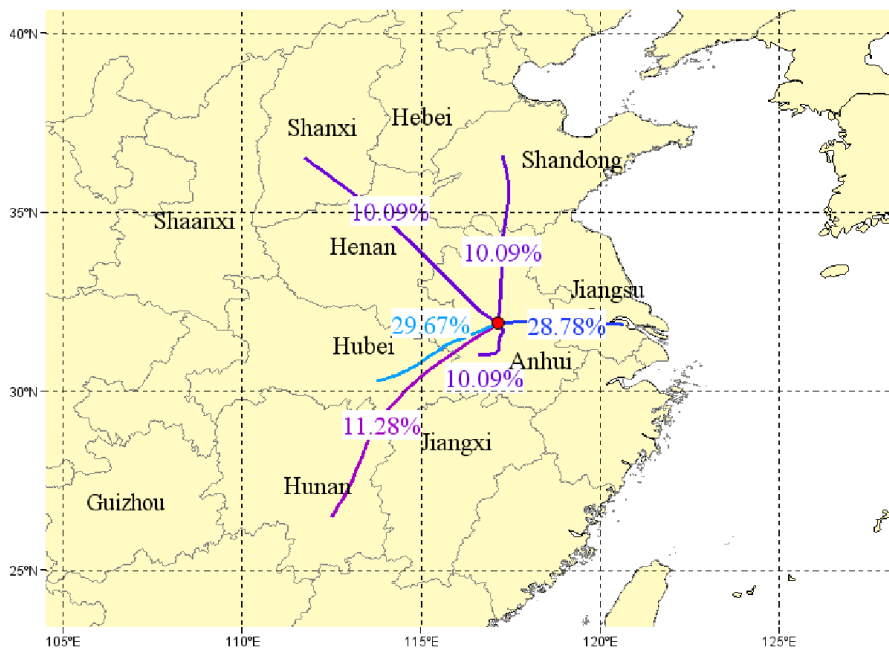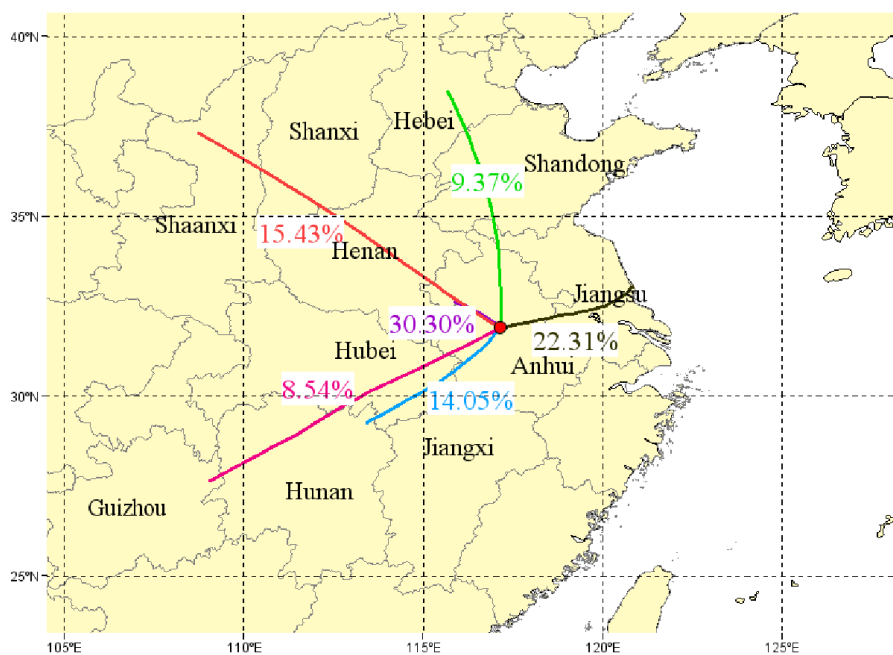
644   Figure 2. One-day HYSPLIT back trajectory clusters arriving at Hefei at 1500 m a.s.l that are

645   coincident with the FTS measurements from 2014 - 2017. (a) Spring and summer (MAM/JJA),

646   and (b) Autumn and winter (SON/DJF) season. The base map was generated using the TrajStat

647   1.2.2 software (http://www.meteothinker. com).
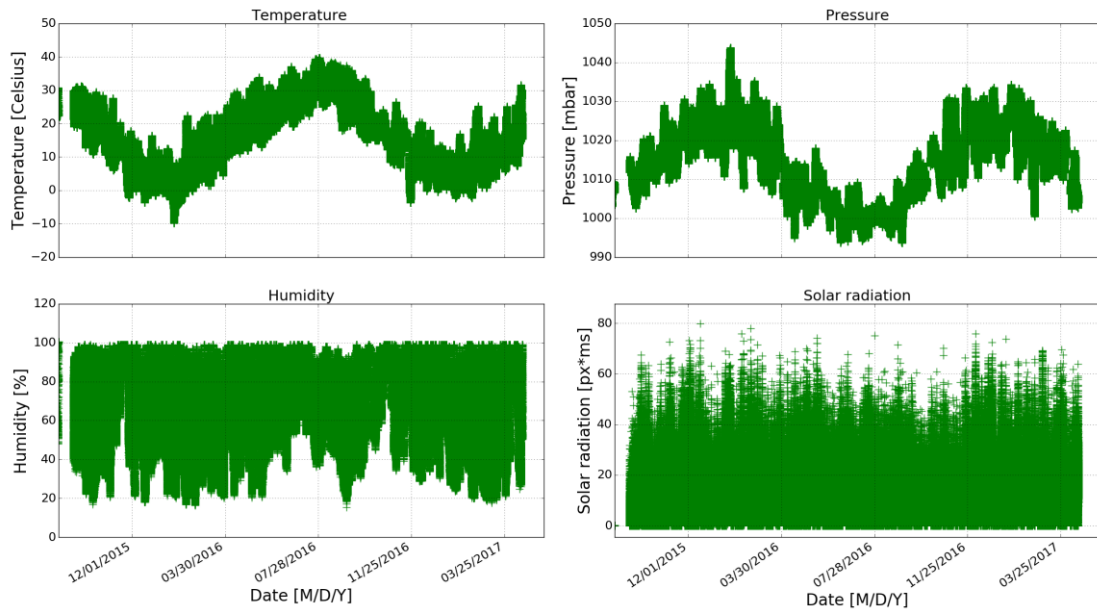
648
649 Figure 3. Minutely averaged time series of temperature, pressure, humidity, and solar radiation
650 recorded by the surface weather station.
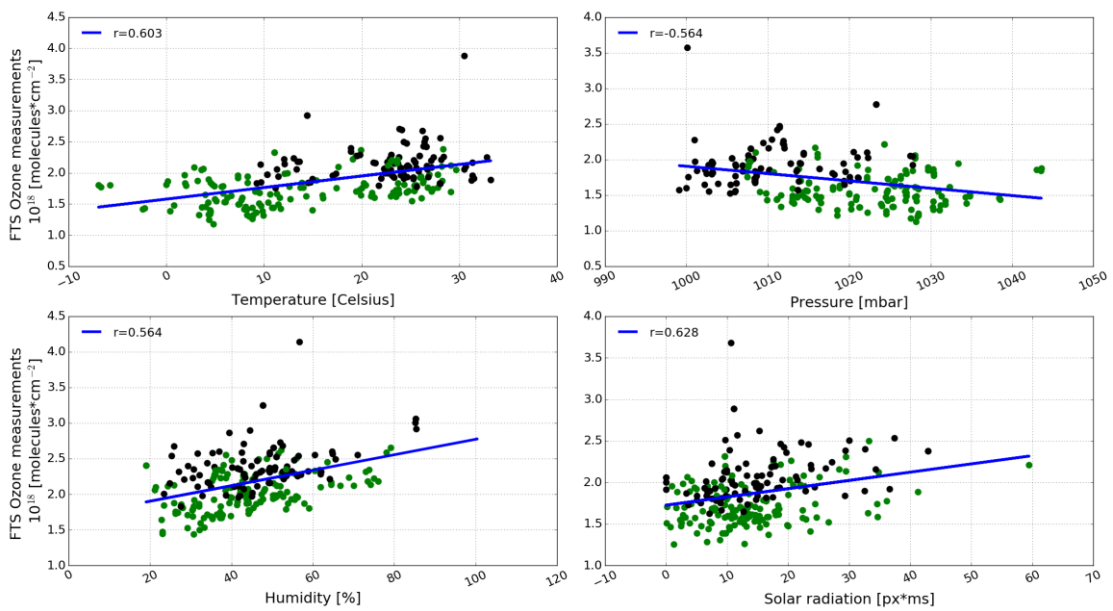
651
652 Figure 4. Correlation plot between the FTS tropospheric O₃ column and the coincident surface
653 meteorological data. Black dots are data pairs within MAM/JJA season and green dots are data
654 pairs within SON/DJF season.
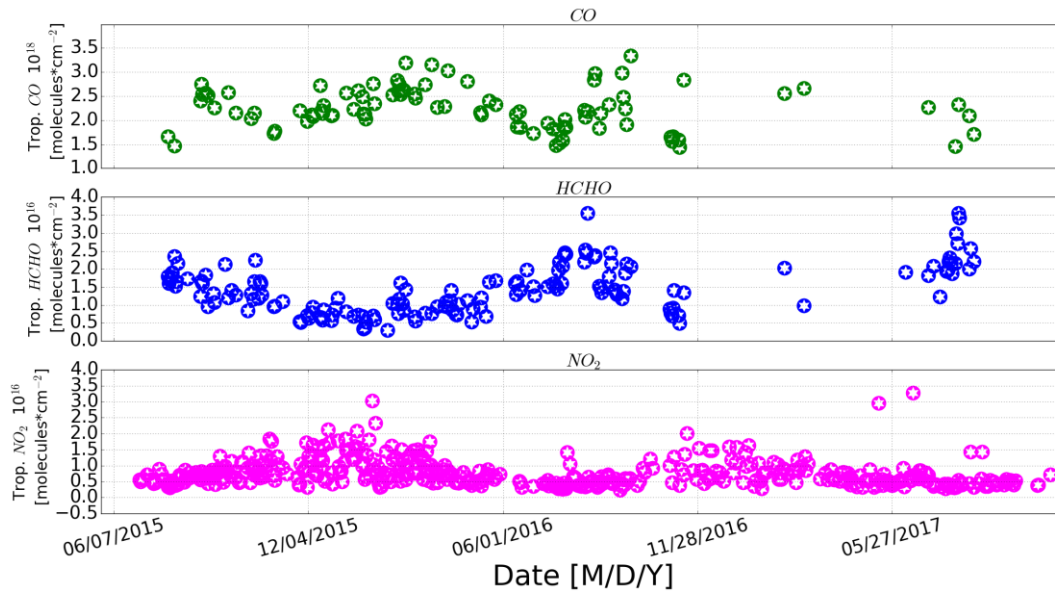
655

656 Figure 5. Time series of tropospheric CO, HCHO, and NO_2. Tropospheric CO and HCHO were

657 derived from FTS observations which is the same as tropospheric O_3 and tropospheric NO_2 is

658 derived from OMI data.

659

660

661

662

663
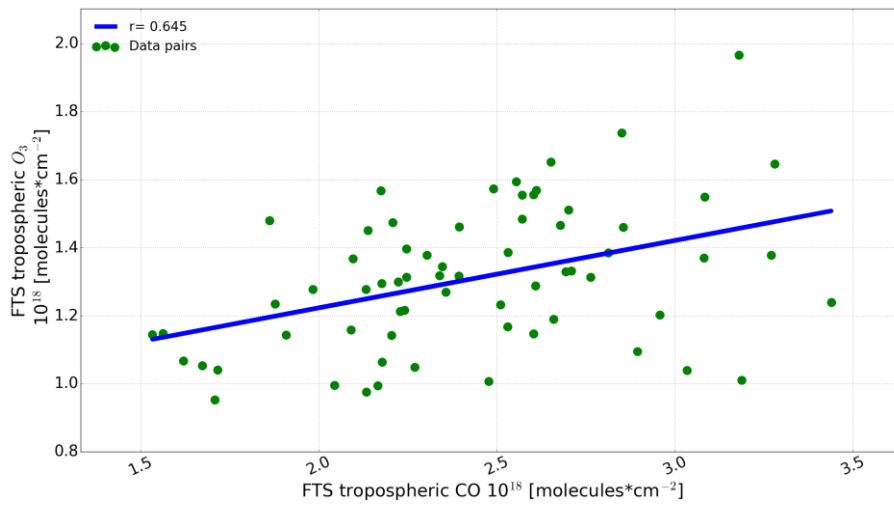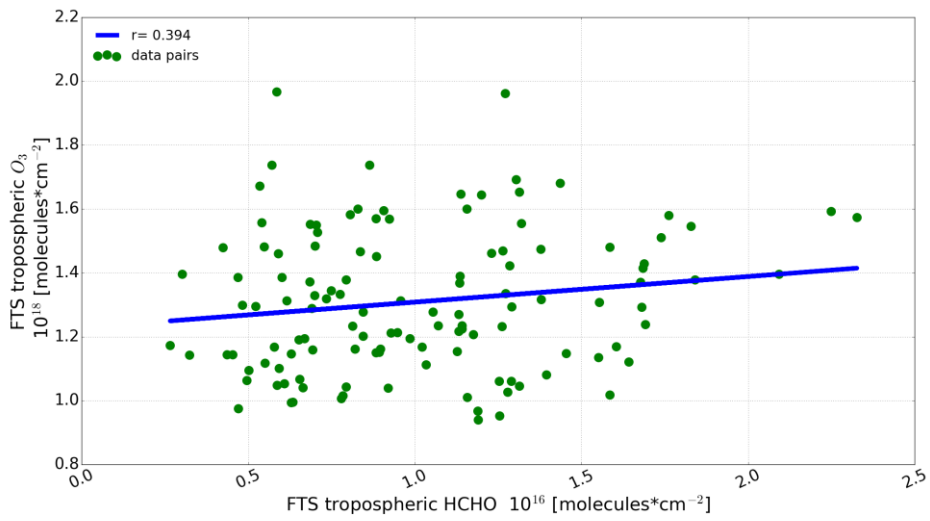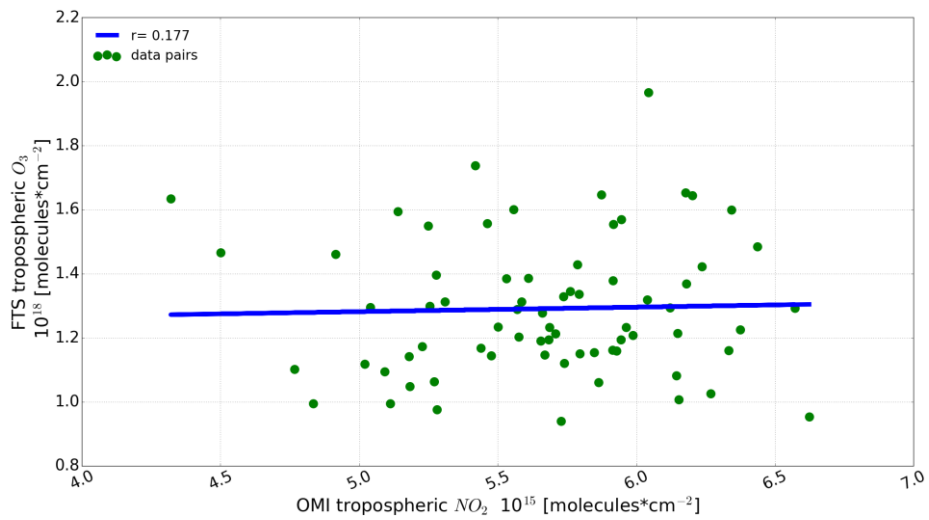
Figure 6. Correlation plot between the FTS tropospheric O_3 column and coincident tropospheric
CO (upper), HCHO (middle), and NO_2 (bottom) columns. The CO and HCHO data are retrieved
from FTS observations and the NO_2 data were deduced from OMI product.
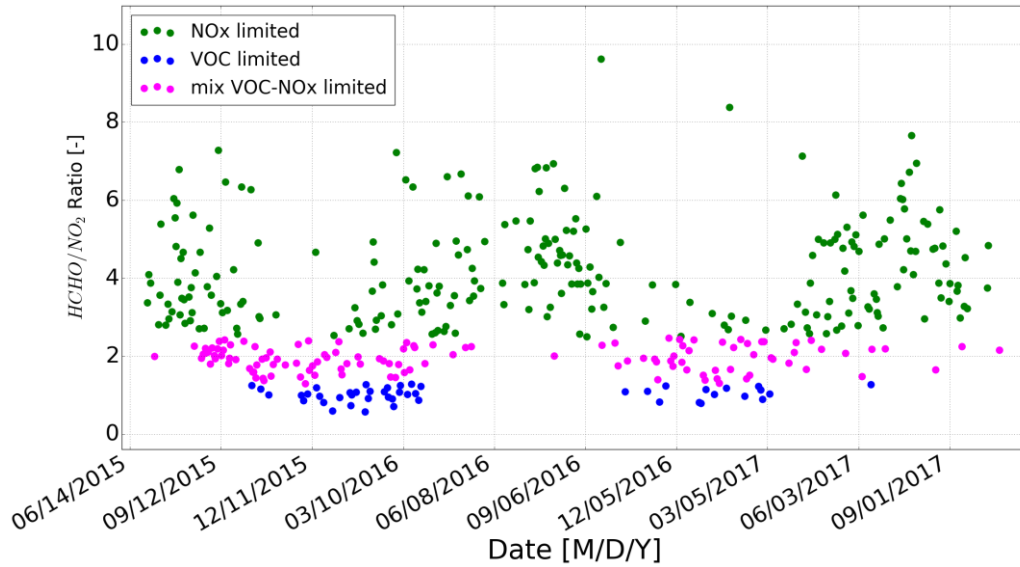
667

668 Figure 7. Time series of column HCHO/NO₂ ratios.

669

Tables

671 Table 1. Summary of the retrieval parameters used for O₃, CO, and HCHO. All micro windows (MW) are
672 given in cm⁻¹.

Gases		O₃	CO	HCHO
Retrieval code		SFIT4 v 0.9.4.4	SFIT4 v 0.9.4.4	SFIT4 v 0.9.4.4
Spectroscopy		HITRAN2008	HITRAN2008	HITRAN2008
P, T, H₂O profiles		NCEP	NCEP	NCEP
A priori profiles for target/interfering gases except H₂O		WACCM	WACCM	WACCM
MW for profile retrievals		1000-1004.5	2057.7-2058 2069.56-2069.76 2157.5-2159.15	2763.42-2764.17 2765.65-2766.01 2778.15-2779.1 2780.65-2782.0
Retrieved interfering gases		H₂O, CO₂, C₂H₄, ⁶⁶⁸O₃, ⁶⁸⁶O₃	O₃, N₂O, CO₂, OCS, H₂O	CH₄, O₃, N₂O, HDO
SNR for de-weighting		None	500	600
Regularization	S_a	Diagonal: 20% No correlation	Diagonal: 11% ~ 27% No correlation	Diagonal: 10% No correlation
	S_ε	Real SNR	Real SNR	Real SNR
ILS		LINEFIT145	LINEFIT145	LINEFIT145
Error analysis		Systematic error: -Smoothing error (smoothing) -Errors from other parameters: Background curvature (curvature), Optical path difference (max_opd), Field of view (omega), Solar line strength (solstrnth), Background slope (slope), Solar line shift (solshft), Phase (phase), Solar zenith angle(sza), Line temperature broadening (linetair_gas), Line pressure broadening (linepair_gas), Line intensity(lineint_gas)		
		Random error: -Interference errors: retrieval parameters (retrieval_parameters), interfering species (interfering_species) -Measurement error (measurement) - Errors from other parameters: Temperature (temperature), Zero level (zshift)		

673
674
675
676
677

678 Table 2. Typical degrees of freedom for signal (DOFs) and sensitive range of the retrieved O₃, CO, and HCHO
679 profiles at Hefei site.

Gas	Total column DOFs	Sensitive range (km)	Tropospheric partial column (km)	Tropospheric DOFs
O₃	4.8	Ground - 44	Ground - 12	1.3
CO	3.5	Ground - 27	Ground - 12	2.7
HCHO	1.2	Ground - 18	Ground - 12	1.1

680

681 Table 3. Errors in % of the column amount of O₃, CO, and HCHO for 0 – 12 km tropospheric partial column and
682 for the total column.

Gas	O₃		CO		HCHO	
Altitude (km)	0 – 12	Total column	0 – 12	Total column	0 – 12	Total column
Total random	3.2	0.59	3.8	0.66	3.3	0.97
Total systematic	8.1	4.86	5.7	3.9	9.6	5.7
Total errors	8.7	5.0	6.8	3.95	10.2	5.8

683

684

685 Table 4. Chemical sensitivities of PO₃ for the selected 106 days of observations that have coincident O₃, HCHO,
686 and NO₂ counterparts

Items	Proportion		Autumn and winter		Spring and summer	
	days	percentage	days	percentage	days	percentage
NOx limited	64	60.3%	19	29.7%	45	70.3%
Mix VOC-NOx limited	30	28.3%	21	70%	9	30%
VOC limited	12	11.4%	9	75%	3	25%
Sum	106	100%	49	46.2%	57	53.8%

687
688